An immersed boundary-thermal lattice Boltzmann method using an equilibrium internal energy density approach for the simulation of flows with heat transfer

H.K. Jeong [a], H.S. Yoon [b], M.Y. Ha [a,*], M. Tsutahara [c]

[a] School of Mechanical Engineering, Pusan National University, San 30, Jang Jeon Dong, Geum Jeong Gu, Busan 609-735, Republic of Korea
[b] Advanced Ship Engineering Research Center, Pusan National University, San 30, Jang Jeon Dong, Geum Jeong Gu, Busan 609-735, Republic of Korea
[c] Graduate School of Science and Technology, Kobe University, Rokkodai, Nada, Kobe 657-8501, Japan

ARTICLE INFO

ABSTRACT

In present paper, a novel immersed boundary-thermal lattice Boltzmann method by the name of "an equilibrium internal energy density approach" is proposed to simulate the flows around bluff bodies with the heat transfer. The main idea is to combine the immersed boundary method (IBM) with the thermal lattice Boltzmann method (TLBM) based on the double population approach. The equilibrium internal energy density approach based on the equilibrium velocity approach [X. Shan, H. Chen, Lattice Boltzmann model for simulating flows with multiple phases and components, Phys. Rev. E 47 (1993) 1815] is used to combine IBM with TLBM. The idea of the equilibrium internal energy density approach is that the satisfaction of the energy balance between heat source on the immersed boundary point and the amount of change of the internal energy density according to time ensures the temperature boundary condition on the immersed boundary. The advantages of this approach are the simple concept, easy implementation and the utilization of original governing equation without modification. The simulation of natural convection in a square cavity with various body shapes for different Rayleigh numbers has been conducted to validate the capability and the accuracy of present method on solving heat transfer problems. Consequently, the present results are found to be in good agreement with those of previous studies.

1. Introduction

Recently, many researchers have adapted various models using the standard lattice Boltzmann method (LBM) to describe the physical phenomenon of fluid. Unlike conventional numerical methods that find solutions of the Navier–Stokes equation based on the macroscopic continuum system, the LBM is based on the kinetic theory of gases and can be characterized as a mesoscopic approach [1].

The LBM uses gas dynamics and represents flow characteristics due to variation of single particle distributions. The LBM is numerically stable and computationally efficient, and highly accurate. Although with these advantages, the LBM still has a few weak points that limit it as a practical computational fluid dynamics tool. One of these shortcomings is the lack of a satisfactory thermal lattice Boltzmann model to solve heat transfer problems like in conventional methods. Many researchers

---

have proposed various thermal lattice Boltzmann models to come with satisfactory solutions for thermal phenomenon problems.

In general, the current thermal models can be classified into three categories: the multi-speed model, the passive-scalar model, the double population model. The multi-speed model is an approach based on the isothermal lattice Boltzmann model which is extended only using density distribution function [2–4]. This model suffers from severe numerical instability and can be simulated in only a narrow temperature range. The passive-scalar model enhanced the numerical stability compared with the multi-speed model. In this model, the temperature was simulated using a separate distribution function, which is independent of the density distribution and the temperature evolution equation is the same as a passive scalar under the condition of negligible viscous heat dissipation and pressure work [5,6]. The double population model proposed by He et al. [7] can be derived from discretization of the continuous evolution equation for the internal energy distribution function in the same way the isothermal LBM was derived in temporal, spatial and momentum spaces. The double population model uses an independent distribution function to calculate a variation of temperature. This model is similar to the passive-scalar model from this point of view. However, it has enhanced numerical stability and contains the effects of viscous heat dissipation and pressure work for considering passive-scalar model.

Another one of shortcomings of standard LBM is that it is not easy to implement the complex physical geometries owing to the constraints such as the regular square grid system with a uniform size and a constant time step. In order to overcome these problems, He et al. [8] proposed the interpolation-supplemented model (IS-LBM) and Shu et al. [9] proposed the Taylor-series-expansion and least-squares-based model. The former model overcomes the shortcoming by preserving the time accuracy of the standard LBM using the time-dependent interpolation scheme between the lattice points and physical geometry. However, it has an extra computational effort for interpolation at every time step and has a restriction of the selecting interpolation scheme. Latter one can be consistently used in any type of lattice model. The final form of this algebraic formulation depends on the coordinate of the mesh points and the lattice velocity, which are different from that in IS-LBM. However this model has some problem in three-dimensional case, because this model needs to save a big matrix with geometry information. On the other hand, there are two other approaches that more directly tackle complex geometries and which have significant impact: (i) interpolated bounce back (IBB) approaches [10–12] and their generalization as a multireflection boundary scheme [13], (ii) volumetric bounce back schemes (VBB) [14–16]. These try to introduce cut-cell or subgrid geometric information.

As another approach, the immersed boundary method (IBM) developed by Peskin [17–19] can be introduced for overcoming the lack of a uniform lattice arrangement originated from the standard LBM, which complicates the simulation of the flow around a complex shape body. As a computational fluid dynamics are applied to engineering problems as well as fundamental fluid mechanics, complex geometries and moving boundaries became one of the main issues. From this point of view, IBM can be considered to be a solution for both problems [20]. Although complex geometries and moving boundaries can be handled by an unstructured grid in the conventional numerical methods (FDM, FEM, and FVM), IBM has its own advantages over the standard LBM. Since IBM is implemented using Cartesian coordinates, it allows the standard LBM to keep its own accuracy. Computational costs and memory requirements are reduced and grid generation is easy. Even for moving bodies, the grid does not have to be regenerated [20].

In the immersed boundary method, two main forms of the acting force have been proposed thus far – direct forcing and feedback forcing. The direct method determines the forces based on the balance of the discretization equations after imposing the desired velocities in the inertial term.

Otherwise, the feedback method treats the boundary as a deformable one with high stiffness. In this study, the feedback forcing method is implemented. The feedback method has been used by Peskin [17–19,18], Goldstein et al. [21,22], Goldstein and Tuan [23], Saiki and Biringen [24], and Lee [25]. Peskin [17,18] used momentum forcing to simulate the flow in a moving heart on the Cartesian grid. Goldstein and his colleagues [21–23] used a spectral code to imitate scalloped shape ribs. Although their method exhibited reasonable results, its suitability for more complicated shapes appears questionable considering the severe limitations of the time step.

On the other hand, since the forces are applied on grid points, the exact simulations of the surfaces do not coincide exactly with the computational grid points; this causes the method to suffer from an interpolation deficiency. This difficulty becomes more pronounced when pressures or viscous forces at the surfaces are desired since the surface location is not well determined. Lee [25] analyzed the stability of Saiki and Biringen's [24] method and found that the linear interpolation of the virtual boundary velocity and the subsequent spreading of the virtual forcing relax the time-step limit for stability by up to four times. Through his analysis, the main disadvantage of the large time-step limit for stability in the feedback method could be overcome.

The details of the feedback method can be found in Saiki and Biringen [24], which provides a detailed explanation of the IBM and summarizes the collaborative researches over thirty years, mainly in the field of biological fluid dynamics. The IBM is still being developed for complex geometries, moving boundaries, multiphase flows, and fluid–structure interaction.

Feng and Michaelides [26,27] proposed the immersed boundary lattice Boltzmann method (IB-LBM). In this approach, the restitution force due to deformation is calculated by the direct methods. In order to improve the numerical stability of the IB-LBM proposed by Feng and Michaelides [26,27], Niu et al. [28] proposed the momentum-exchange-based immersed boundary lattice Boltzmann method by using the multi-relaxation collision model. This approach is a simpler and efficient method for calculating the body force at immersed boundary points. Shu et al. [29] proposed the immersed boundary velocity correction method (IBVCM). This method used the concept of the fractional step technique and is equivalent to make a

correction in the velocity field from the adding a body force in the momentum equations. In addition, because the IBM can be easily implemented to the LBM and has a great potential for moving boundary problems such as the particulate flows and the deformable objects in fluids [30], many researchers have enhanced the computational efficiency and accuracy of the IB-LBM [30–32]. These methods to incorporate the IBM into the LBM enhanced the capability of LBM for isothermal problems only whereas many engineering problems have the thermal phenomena. Thus we need a new approach to solve the thermal problems using the IBM.

As above mentioned, there are numerous researches for the IB-LBM with direct forcing scheme [26–32]. However, based on the authors' survey of literature, it is hard to find that a literature has dealt with IB-LBM with feedback forcing scheme and especially IB-thermal LBM with feedback forcing scheme. In spite of the well known shortcomings of the feedback forcing scheme, it is worth to be further developed due to the simplicity of this scheme to be adopted into the different numerical methods such as the finite-types methods and LBM. Consequently, the purpose of this study is the implement of the feedback forcing scheme to the thermal LBM.

A body force acting on the immersed boundary is included in the governing equation as an external force. Shan and Chen [33] introduced the concept of "equilibrium velocity" to consider the momentum change produced by the body force. The equilibrium velocity included in the equilibrium density distribution function acts as a change of momentum. In this study, unlike the IB-LBM proposed by of Feng and Michaelides [26,27], we included the external force in terms of the equilibrium velocity proposed by Shan and Chen [33]. The IBM and LBM were combined using this alternative scheme with the equilibrium velocity concept which differs from that of Feng and Michaelides [26,27] for the momentum calculation. In order to consider the heat transfer, we selected the same manner with the equilibrium velocity approach to calculate the thermal lattice Boltzmann method using the double population approach proposed by He et al. [7]. In order to combine the IBM and thermal LBM, we introduced an "equilibrium internal energy density" as a function of internal energy density and heat source.

This paper is organized as follows. Section 2 reviews the 9-bit thermal LBM with the double population approach and the feedback forcing method is explained and the calculation procedure used for implementing the equilibrium velocity and the equilibrium internal energy density with immersed boundary forcing is introduced. Section 3 presents the numerical results of the simulation of the flow in two-dimensional natural convection problems with circular or square cylinder in a square enclosure using the thermal LBM. Section 4 concludes the paper.

2. Immersed boundary-thermal LBM

2.1. The thermal LBM

The governing equation of the LBM originates from the Boltzmann equation, expanding a basic formulation of lattice gas automata (LGA) to the real number range; the LBM enhanced its application scope and numerical stability. Because the LBM is derived from the LGA, the LB equation is introduced beginning from a discrete kinetic equation for the particle distribution function:

$$f_i(\mathbf{x} + \mathbf{c}_i \delta t, t + \delta t) = f_i(\mathbf{x}, t) + \Omega_i. \tag{1}$$

In this equation, f_i, $\mathbf{c}_i$, Ω_i, $\mathbf{x}$ and δt are the density distribution function, Cartesian component of ith lattice velocity, collision operator along the ith direction, position vector along the Cartesian coordinate and time increment, respectively. The subscript i is the particle direction which depends on the lattice model. The collision operator represents a proportion, which particle distribution would be changed by a collision process. It should be pointed out that the position vector and the lattice velocity vector are independent. The mathematical description of the underlying physical phenomena involved in collision process is, in general, very complex. According to a single relaxation time model proposed by Bhatnagar, Gross and Krook (BGK), the collision operator is simplified. Hence the lattice BGK equation is

$$\Omega_i = -\frac{1}{\tau} \left(f_i(\mathbf{x}, t) - f_i^{eq}(\mathbf{x}, t) \right), \tag{2}$$

where f_i^{eq} is the equilibrium density distribution function, and τ is the single relaxation time which controls the rate of approach from the non-equilibrium to the equilibrium state. If the Boltzmann equation is discretized by time and the velocity at Navier–Stokes level, the final discretized equation would be an isothermal lattice Boltzmann equation. This process is adapted to Boltzmann energy equation. The results by discretization using this process are the thermal lattice Boltzmann equation which describes the macroscopic temperature variation. The double population approach proposed by He et al. [7] is used as the thermal model in this study. In this model, the governing equation can be separated as an internal energy density distribution g_i and the density distribution f_i to solve the temperature field and flow field, respectively,

$$\bar{f}_i(\mathbf{x} + \mathbf{c}_i \delta t, t + \delta t) - \bar{f}_i(\mathbf{x}, t) = -\frac{\delta t}{\tau_f + 0.5\delta t} \left[\bar{f}_i(\mathbf{x}, t) - f_i^{eq}(\mathbf{x}, t) \right] + \frac{\tau_f \delta t}{\tau_f + 0.5\delta t} F_i, \tag{3}$$

$$\bar{g}_i(\mathbf{x} + \mathbf{c}_i \delta t, t + \delta t) - \bar{g}_i(\mathbf{x}, t) = -\frac{\delta t}{\tau_g + 0.5\delta t} \left[\bar{g}_i(\mathbf{x}, t) - g_i^{eq}(\mathbf{x}, t) \right] + \frac{\tau_g \delta t}{\tau_g + 0.5\delta t} f_i Z_i. \tag{4}$$

The new variables $\bar{f}_i$ and $\bar{g}_i$ are defined as

$$\bar{f}_i = f_i + \frac{0.5\delta t}{\tau_f}(f_i - f_i^{eq}),$$ (5)

$$\bar{g}_i = g_i + \frac{0.5\delta t}{\tau_g}(g_i - g_i^{eq}) + \frac{\delta t}{2}f_iZ_i,$$ (6)

$$g_i = \frac{(\mathbf{c}_i - \mathbf{u})^2}{2}f_i.$$ (7)

Here, g_i^{eq} is the equilibrium internal energy density distribution function. τ_f and τ_g are the relaxation times. Time increment and lattice space are $\delta t = \delta x = 1$. Z_i represents the effects of viscous heating in Eq. (8)

$$Z_i = (\mathbf{c}_i - \mathbf{u}) \cdot [\partial\mathbf{u}/\partial t + (\mathbf{c}_i \cdot \nabla)\mathbf{u}],$$ (8)

$$F_i = \frac{\mathbf{G} \cdot (\mathbf{c}_i - \mathbf{u})}{RT}f_i^{eq},$$ (9)

F_i is a body force and corresponded to the buoyancy force in this study in Eq. (9). $\mathbf{G}$ means the body force acting per unit mass.

In all the simulations, a two-dimensional D2Q9 model was used. The equilibrium density distribution function and equilibrium internal energy density distribution function [7] can be written as follows:

$$f_i^{eq} = \omega_i\rho\left[1 + \frac{3\mathbf{c}_i \cdot \mathbf{u}}{c^2} + \frac{9(\mathbf{c}_i \cdot \mathbf{u})^2}{2c^4} - \frac{3\mathbf{u}^2}{2c^2}\right],$$ (10)

$$g_i^{eq} = \omega_i\rho\varepsilon\left[\frac{3(\mathbf{c}_i^2 - \mathbf{u}^2)}{2c^2} + 3\left(\frac{3\mathbf{c}_i^2}{2c^2} - 1\right)\frac{(\mathbf{c}_i \cdot \mathbf{u})}{c^2} + \frac{9(\mathbf{c}_i \cdot \mathbf{u})^2}{2c^4}\right].$$ (11)

The discrete velocity space for D2Q9 model is

$$\mathbf{c}_i = \begin{cases} 0 & i = 0, \\ (\cos[(i-1)\pi/2], \ \sin[(i-1)\pi/2])c & i = 1,2,3,4, \\ \sqrt{2}(\cos[(i-5)\pi/2 + \pi/4], \ \sin[(i-5)\pi/2 + \pi/4])c & i = 5,6,7,8, \end{cases}$$ (12)

where ω_i is a weighting coefficient, $\omega_0 = 4/9$, $\omega_i = 1/9$ for $i = 1,2,3,4$ and $\omega_i = 1/36$ for $i = 5,6,7,8$. ε is the internal energy, that satisfies $\rho\varepsilon = \rho RT$. In the thermal model, the lattice speed is $c = \sqrt{3RT_0}$. T_0 is the averaged temperature and R is the gas constant.

The macroscopic density (ρ), velocity ($\mathbf{u}$), internal energy per unit mass (ε) can be obtained from the following equations of constraints in Eq. (13). The heat flux is Eq. (14). Kinematic viscosity and thermal diffusivity is Eq. (15)

$$\rho = \sum_i \bar{f}_i,$$

$$\rho\mathbf{u} = \sum_i \bar{f}_i\mathbf{c}_i,$$ (13)

$$\rho\varepsilon = \sum_i \bar{g}_i - \frac{\delta t}{2}\sum_i f_iZ_i,$$

$$\mathbf{q} = \left(\sum_i \mathbf{c}_i\bar{g}_i - \rho\varepsilon\mathbf{u} - \frac{\delta t}{2}\sum_i \mathbf{c}_if_iZ_i\right)\frac{\tau_g}{\tau_g + 0.5\delta t},$$ (14)

$$v = \tau_f RT_0, \quad \alpha = 2\tau_g RT_0.$$ (15)

2.2. Feedback immersed boundary method

Immersed boundary points generally do not coincide with the lattice nodes. The immersed boundary points are coupled with the lattice nodes by an interpolation scheme. Then, the velocity information on the object's surface is obtained from its position. As shown in Fig. 1, the interpolation scheme uses four lattice points (i.e. forcing points) adjacent to the immersed boundary point. The exact velocity on the immersed boundary node is calculated by a bilinear interpolation scheme. Bilinear interpolation is used to determine the surface velocities with their position information. Momentum forcing is evaluated using the feedback algorithm. The velocity difference between the desired velocity and the current velocity at the immersed boundary is controlled to be minimized as time advances. The discrete surface points in Fig. 1 are the immersed boundary points, $\mathbf{x}_s(x_s, y_s)$. Therefore, using the bilinear interpolation scheme, the velocity of the immersed boundary points $\mathbf{u}(\mathbf{x}_s)$ is interpolated from the velocities $\mathbf{u}_{i,j}$ at nearby lattice points in Eq. (16)

$$\mathbf{u}(\mathbf{x}_s) = \sum_{i,j}^{i+1,j+1} D_{i,j}(\mathbf{x}_s)\mathbf{u}_{i,j},$$ (16)
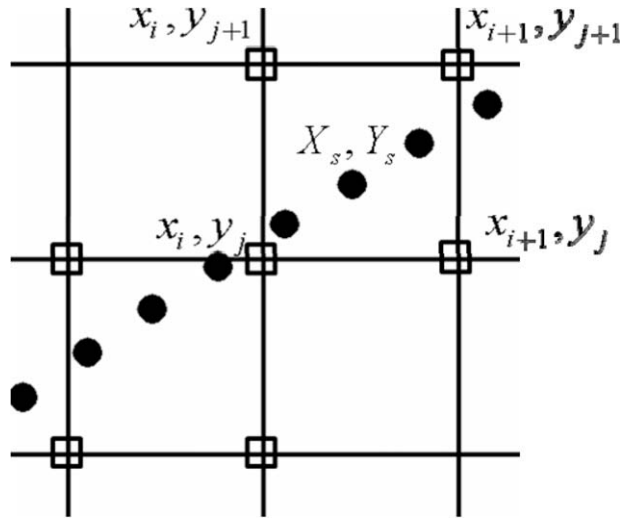
Fig. 1. Forcing points related with immersed boundary points in Cartesian grid system.

where $D_{i,j}(\mathbf{x}_s) = d(x_s - x_i)d(y_s - y_j)$ and the distance ratio (d) between lattice position and immersed boundary point can be expressed as follows:

$$d(x_s - x_i) = \frac{(x_s - x_i)}{(x_{i+1} - x_i)} \quad \text{if } x_i < x_s, \tag{17a}$$

$$d(x_s - x_i) = \frac{(x_s - x_{i-1})}{(x_i - x_{i-1})} \quad \text{if } x_i > x_s, \tag{17b}$$

$$d(x_s - x_i) = 1 \quad \text{if } x_i = x_s. \tag{17c}$$

In order to satisfy the no-slip boundary condition on the surface, the velocity has a feedback relationship with the flow field and it should be converted to a body force. The momentum forcing $\mathbf{F}_m(\mathbf{x}_s, t)$ was proposed by Goldstein et al. [21,22] and Saiki and Biringen [24]. The feedback momentum forcing function $\mathbf{F}_m(\mathbf{x}_s, t)$ can be expressed as

$$\mathbf{F}_m(\mathbf{x}_s, t) = \alpha_f \int_0^t [\mathbf{u}(\mathbf{x}_s, t') - \mathbf{V}(\mathbf{x}_s, t')]dt' + \beta_f[\mathbf{u}(\mathbf{x}_s, t) - \mathbf{V}(\mathbf{x}_s, t)]. \tag{18}$$

Here, the negative constants of α_f and β_f have the dimensions with the reciprocal of time squared and the reciprocal of time, respectively.

The velocity difference $\mathbf{u}(\mathbf{x}_s, t) - \mathbf{V}(\mathbf{x}_s, t)$, which is actually the error, determines the feedback forcing, and the momentum forcing controls the boundary velocity, $\mathbf{u}(\mathbf{x}_s, t)$ to be the same as the desired velocity $\mathbf{V}(\mathbf{x}_s, t)$. If the boundary does not rotate or move, $\mathbf{V}(\mathbf{x}_s, t)$ becomes zero and Eq. (18) reduces to Eq. (19). If the time integral is replaced with the Riemann sum for Eq. (20), we obtain Eq. (21) for the feedback momentum forcing

$$\mathbf{F}_m(\mathbf{x}_s, t) = \alpha_f \int_0^t \mathbf{u}(\mathbf{x}_s, t')dt' + \beta_f[\mathbf{u}(\mathbf{x}, t)], \tag{19}$$

$$\int_0^t \mathbf{u}(\mathbf{x}_s, t')dt' \cong \sum_{j=1}^N \mathbf{u}(\mathbf{x}_s, j)\delta t, \tag{20}$$

$$\mathbf{F}_m(\mathbf{x}_s, t) = \alpha_f \sum_{t'=0}^{t'=t} \mathbf{u}(\mathbf{x}_s, t') + \beta_f[\mathbf{u}(\mathbf{x}_s, t)]. \tag{21}$$

Using Eq. (21), the forcing density $\mathbf{F}_m(\mathbf{x}_s, t)$ at the immersed boundary is calculated and redistributed to the lattice points near the immersed boundary. The sum of nearby forcing density multiplied by the weighting factor yields the momentum forcing $\mathbf{F}_b(\mathbf{x}, t)$ of nearby lattice points as the body force. The weighting factor is given by the interpolation scheme

$$\mathbf{F}_b(\mathbf{x}, t) = \frac{1}{N_b} \sum_{n=1}^{N_b} D_{i,j}(\mathbf{x}_s)\mathbf{F}_m(\mathbf{x}_s). \tag{22}$$

Here, N_b is the number of immersed boundary points that affect the lattice point. The method prescribed above is the "area-weighted" method proposed by Saiki and Biringen [24].

In order to simulate the thermal applications, Eqs. (18) and (22) can be rearranged about the heat source term. The feedback energy forcing density and heat source are expressed as follows:

$$\Phi(\mathbf{x}_s, t) = \alpha_g \int_0^t [\varepsilon(\mathbf{x}_s, t') - \vartheta(\mathbf{x}_s, t')] dt' + \beta_g [\varepsilon(\mathbf{x}_s, t) - \vartheta(\mathbf{x}_s, t)] \tag{23}$$

$$\Theta(\mathbf{x}_\alpha, t) = \frac{1}{N_b} \sum_{n=1}^{N_b} D_{i,j}(\mathbf{x}_s) \Phi(\mathbf{x}_s) \tag{24}$$

where ϑ means desired internal energy on immersed boundary. The heat source Θ is applied to satisfy the thermal boundary condition on the immersed boundary. The coefficients of α_g and β_g are negative constants and they have same dimensions with the coefficients of α_f and β_f, respectively.

2.3. A description of immersed boundary-thermal LBM

Based on the thermal lattice Boltzmann model using the double population approach in which the viscous heat dissipation term is neglected, the governing equations of the thermal lattice Boltzmann method are as follows:

$$\bar{f}_i(\mathbf{x} + \mathbf{c}_i \delta t, t + \delta t) - \bar{f}_i(\mathbf{x}, t) = -\frac{\delta t}{\tau_f + 0.5\delta t} [\bar{f}_i(\mathbf{x}, t) - f_i^{eq}(\mathbf{x}, t)] + \frac{\tau_f \delta t}{\tau_f + 0.5\delta t} F_i, \tag{25}$$

$$\bar{g}_i(\mathbf{x} + \mathbf{c}_i \delta t, t + \delta t) - \bar{g}_i(\mathbf{x}, t) = -\frac{\delta t}{\tau_g + 0.5\delta t} [\bar{g}_i(\mathbf{x}, t) - g_i^{eq}(\mathbf{x}, t)]. \tag{26}$$

If an additional external force $\mathbf{F}_b$ is acting, there is a change of momentum $\Delta \mathbf{P} = \mathbf{F}_b$, ($\mathbf{P} = \rho \mathbf{u}$) at every time step. In order to incorporate this into the model, an equilibrium density distribution can be accomplished by using

$$f_i^{eq^*}(\mathbf{x}, t) = f_i^{eq}(\rho, \mathbf{u}^*) \quad \text{and} \quad \rho \mathbf{u}^* = \rho \mathbf{u} + \frac{\tau_f + 0.5\delta t}{\delta t} \mathbf{F}_b. \tag{27}$$

In this equation, $\mathbf{u}^*$ denotes the "equilibrium velocity", which is given by Shan and Chen [33]. $f_i^{eq^*}$ is the modified equilibrium density distribution function with an equilibrium velocity. After the substitution of Eq. (27) into Eq. (25), multiplying Eq. (25) by $\mathbf{c}_i$, and summing over all directions, the momentum conservation relation with the change in the total momentum at each lattice is obtained

$$\sum_i \mathbf{c}_i \bar{f}_i(\mathbf{x} + \mathbf{c}_i \delta t, t + \delta t) - \sum_i \mathbf{c}_i \bar{f}_i(\mathbf{x}, t) = -\frac{\delta t}{\tau_f + 0.5\delta t} \left(\sum_i \mathbf{c}_i \bar{f}_i(\mathbf{x}, t) - \sum_i \mathbf{c}_i f_i^{eq^*}(\mathbf{x}, t) \right), \tag{28}$$

$$\sum_i \mathbf{c}_i \bar{f}_i(\mathbf{x} + \mathbf{c}_i \delta t, t + \delta t) - \sum_i \mathbf{c}_i \bar{f}_i(\mathbf{x}, t) = -\frac{\delta t}{\tau_f + 0.5\delta t} \left(\sum_i \mathbf{c}_i \bar{f}_i(\mathbf{x}, t) - \left(\sum_i \mathbf{c}_i f_i^{eq}(\mathbf{x}, t) + \frac{\tau_f + 0.5\delta t}{\delta t} \mathbf{F}_b(\mathbf{x}, t) \right) \right), \tag{29}$$

$$\rho(\mathbf{x} + \mathbf{c}_i \delta t, t + \delta t) \mathbf{u}(\mathbf{x} + \mathbf{c}_i \delta t, t + \delta t) - \rho(\mathbf{x}, t) \mathbf{u}(\mathbf{x}, t) = \mathbf{F}_b(\mathbf{x}, t). \tag{30}$$

From Eqs. (28)–(30), the body force is satisfied with the change in momentum $\Delta \mathbf{P} = \mathbf{F}_b$. From Eq. (11), $\sum_i \bar{g}_i = \sum_i g_i^{eq} = \rho \varepsilon$. $\rho \varepsilon$ means an internal energy density and the internal energy is $\varepsilon = DRT/2$ (D: dimension: $D = 2$ in D2Q9 model).

With the same procedure to satisfy the momentum conservation by an additional external force, the immersed boundary with heat transfer can be adapted in the thermal lattice Boltzmann model. In this study, we would select the same manner with the equilibrium velocity approach for the immersed boundary-thermal lattice Boltzmann method.

Now we define an "equilibrium internal energy density ($\rho \varepsilon^*$)" as a function of internal energy density and heat source

$$\rho \varepsilon^* = \rho \varepsilon + \left(\frac{\tau_g + 0.5\delta t}{\delta t} \right) \Theta, \tag{31}$$

where Θ is a heat source. If a heat source Θ is acting, there is a change of internal energy $\Delta \rho \varepsilon = \Theta$ at every time step and the modified equilibrium internal energy density distribution is defined as

$$g_i^{eq^*}(\mathbf{x}, t) = g_i^{eq}(\rho, \varepsilon^*). \tag{32}$$

In this equation ε^* denotes the "equilibrium internal energy". When the modified internal energy density equilibrium distribution is used instead of the internal energy density equilibrium distribution, the change in the internal energy density at each lattice is obtained. Adopting the same method for expanding the internal energy conservation relation,

$$\sum_i \bar{g}_i(\mathbf{x} + \mathbf{c}_i \delta t, t + \delta t) - \sum_i \bar{g}_i(\mathbf{x}, t) = -\frac{\delta t}{\tau_g + 0.5\delta t} \left[\sum_i \bar{g}_i(\mathbf{x}, t) - \sum_i g_i^{eq^*}(\mathbf{x}, t) \right], \tag{33}$$

$$\sum_i \bar{g}_i(\mathbf{x} + \mathbf{c}_i \delta t, t + \delta t) - \sum_i \bar{g}_i(\mathbf{x}, t) = -\frac{\delta t}{\tau_g + 0.5\delta t} \left[\sum_i \bar{g}_i(\mathbf{x}, t) - \left(\sum_i g_i^{eq}(\mathbf{x}, t) + \left(\frac{\tau_g + 0.5\delta t}{\delta t} \right) \Theta(\mathbf{x}, t) \right) \right], \tag{34}$$

$$\rho(\mathbf{x} + \mathbf{c}_i \delta t, t + \delta t)\varepsilon(\mathbf{x} + \mathbf{c}_i \delta t, t + \delta t) - \rho(\mathbf{x}, t)\varepsilon(\mathbf{x}, t)$$

$$= -\frac{\delta t}{\tau_g + 0.5\delta t}\left[\rho(\mathbf{x}, t)\varepsilon(\mathbf{x}, t) - \left(\rho(\mathbf{x}, t)\varepsilon(\mathbf{x}, t) + \left(\frac{\tau_g + 0.5\delta t}{\delta t}\right)\Theta(\mathbf{x}, t)\right)\right], \tag{35}$$

$$\rho(\mathbf{x} + \mathbf{c}_i \delta t, t + \delta t)\varepsilon(\mathbf{x} + \mathbf{c}_i \delta t, t + \delta t) - \rho(\mathbf{x}, t)\varepsilon(\mathbf{x}, t) = \Theta(\mathbf{x}, t). \tag{36}$$

From Eqs. (33)–(36), the heat source is satisfied with the change in internal energy density $\Delta\rho\varepsilon = \Theta$.

2.4. Boundary conditions

In order to satisfy the no-slip and constant temperature boundary condition, the non-equilibrium first order extrapolation boundary condition proposed by Guo et al. [34] and the internal energy non-equilibrium first order extrapolation boundary condition by Tang et al. [35] are used:

$$\bar{f}_i^+(O, t) = f_i^{eq}(\rho(B), \mathbf{u}(O), t) + (1 - \omega_f)[\bar{f}_i(B, t) - f_i^{eq}(B, t)], \tag{37}$$

$$\bar{g}_i^+(O, t) = g_i^{eq}(\rho(B), \mathbf{u}(O), T(O), t) + (1 - \omega_g)[\bar{g}_i(B, t) - g_i^{eq}(B, t)], \tag{38}$$

where $\omega_{f,g} = \delta t/(\tau_{f,g} + 0.5\delta t)$, and '+' denotes the 'after collision step'.

Fig. 2 represents the direction and distribution of particles near the wall. As shown in Fig. 2, the DOA line is the wall boundary satisfying no-slip, and the FBE line lies in the fluid. C_i is the direction of the particle. In this study, the non-equilibrium first order extrapolation boundary condition needs only the value f_i at node B. As shown in Eq. (37), because $\rho(O)$ at the wall is unknown, Guo et al. [34] substituted $\rho(B)$ at node B into $\rho(O)$. Also Tang et al. [35] used a process similar to Guo et al. [34]. Because the density at the wall node $\rho(O)$ is calculated when $\bar{f}_i$ is calculated, $\rho(O)$ is also known in $\bar{g}_i$. Therefore the internal energy equilibrium density function g^{eq} proposed by Tang et al. [35] is modified like Eq. (39). Also Eq. (38) modified using this process can be Eq. (40).

$$g_i^{eq}(O, t) = g_i^{eq}(\rho(O), \mathbf{u}(O), T(O), t), \tag{39}$$

$$\bar{g}_i^+(O, t) = g_i^{eq}(\rho(O), \mathbf{u}(O), T(O), t) + (1 - \omega_g)[\bar{g}_i(B, t) - g_i^{eq}(B, t)]. \tag{40}$$

3. Numerical results and discussion

3.1. Natural convection in a square enclosure

For the purpose of thermal LBM code validation, the natural convection problem in a vertical/horizontal enclosure without a body was tested. The configuration of the natural convection in a vertical enclosure (VE) given by de Vahl Davis [36] consists of a 2-D square cavity with a hot wall on the left and a cold wall on the right side and other side walls are adiabatic (see Fig. 3(a)). For the pure Rayleigh–Bénard convection in a horizontal enclosure (HE), the bottom and top wall are kept at the hot and cold temperatures and the left and right walls are adiabatic (see. Fig. 3(b)). The natural convection and pure Rayleigh–Bénard convection have vertical/horizontal temperature gradients. The Rayleigh number (Ra) of the flow is defined by Eq. (41) where $\Delta T = T_H - T_L$ is the temperature difference between the hot and cold walls. Prandtl number (Pr) is fixed at
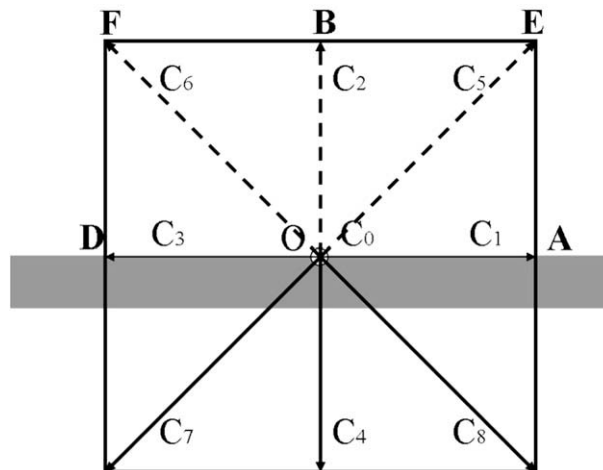

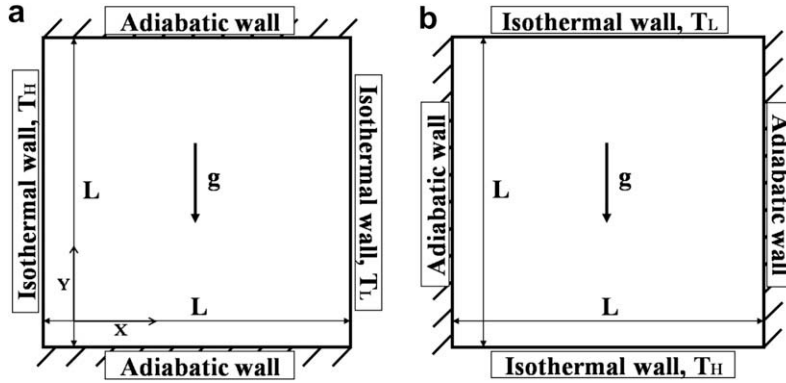**Fig. 2.** Schematic plot of particle velocity at a wall boundary.

Fig. 3. Schematics of natural convection (a) and pure Rayleigh–Bénard convection (b).

0.71. The computational domain and boundary condition is shown in Fig. 3. The height and width between the walls with different temperatures are L

$$Ra = \frac{g\beta\Delta TL^3}{\nu\alpha} = \frac{\left(\sqrt{g\beta\Delta TL}\right)^2 L^2}{\nu\alpha}, \quad Pr = \frac{\nu}{\alpha}. \tag{41}$$

The advance/backward difference law which has a second order accuracy was applied to the insulated adiabatic walls for each case. For all cases, a 129×129 uniform grid was used for the $Ra = 10^3$ and 10^4 and a 205×205 uniform grid was used for the $Ra = 10^5$ and 10^6.

The external force term **F** corresponding to the buoyancy force was given by Eq. (42) where **G** is the external force acting per unit mass. β and g are the thermal expansion coefficient and acceleration due to gravity. **j** denotes the opposite direction of gravity

$$\mathbf{F} = \frac{\mathbf{G}\cdot(\mathbf{c}_i - \mathbf{u})}{RT}f_i^{eq}, \quad \rho\mathbf{G} = \rho\beta g(T - T_0)\mathbf{j}. \tag{42}$$

To simulate natural convection using the Boussinesq approximation, the viscous heat dissipation term is negligible. When Rayleigh number is defined as Eq. (41), g and β are still unknown. He et al. [7] defined the characteristic velocity as $V_c = \sqrt{\beta g\Delta TL}$. The characteristic velocity was included in the body force term and plays the role of controlling the effect of gravity not only the collision but also the constraints process. Also the characteristic velocity depends on the characteristic length, the shape of computational domain and the gravity effect. Therefore the characteristic velocity should be determined carefully. In this study, the relation between the characteristic velocity, thermal diffusivity, Ra, Pr is shown in Eq. (43). The single relaxation times τ_f and τ_g are defined by Eq. (44), respectively

$$\frac{\alpha}{L} = \frac{\sqrt{\beta g\Delta TL}}{\sqrt{RaPr}}, \tag{43}$$

$$\tau_f = \frac{V_cL}{RT_0}\sqrt{\frac{Pr}{Ra}}, \quad \tau_g = \frac{V_cL}{2RT_0\sqrt{Ra\,Pr}}. \tag{44}$$

Fig. 4 shows streamlines and isotherms of each case within the range of $Ra = 10^3 - 10^6$. Fig. 5 shows the variation of normalized temperature profiles, along the horizontal centerline ($y/L = 0.5$) of the square cavity for Ra ranging from 10^3 to 10^6 for the natural convection problem in a vertical enclosure.

Table 1 compares the results from the present simulation with previous results [36–38]. The surface-averaged Nusselt numbers ($\overline{Nu}$) at the hot wall for each case was compared for Ra less than 10^6. The present results agree well with those of other researchers. Comparing with the results using the multi-domain spectral method with high accuracy, the maximum error is 0.61% and 0.46% respectively. The local Nusselt number (Nu) and surface-averaged Nusselt number ($\overline{Nu}$) at the hot wall is defined by Eq. (45)

$$Nu = -\frac{L}{\Delta T}\frac{\partial T}{\partial n}\bigg|_{Hot\ wall}, \quad \overline{Nu} = \frac{1}{L}\int_0^L Nu\,ds, \tag{45}$$

where n is the normal direction to walls.

3.2. Natural convection with various shaped body in a square enclosure

3.2.1. Natural convection in a square enclosure with a circular cylinder

A schematic diagram of the computational geometry in 2-dimensional plane with uniform grid distribution is shown in Fig. 6(a). The system consists of a square enclosure with sides of length L and a stationary circular cylinder is located in the centre ($x = y = 0$) of square enclosure with $R = 0.2L$. The walls of the square enclosure were kept at a constant low temperature of T_c whereas the cylinder was kept at a constant high temperature of T_h. The fluid properties are also assumed to be constant, except for the density in the buoyancy term, which follows the Boussinesq approximation of Eq. (42). The gravitational acceleration acts in the negative y-direction. The immersed boundary method is used to handle the inner circular cylinder in Cartesian coordinates. In these simulations to be reported here the Prandtl number has been taken to be 0.71 and Rayleigh number varies in the range of 10^3–10^6. The characteristic velocity is fixed at $V_c = 0.01c$ for $Ra = 10^3$, whereas $V_c = 0.1c$ was used for $Ra = 10^4$–10^6. A 101×101 uniform grid was used for $Ra = 10^3$, whereas a 201×201 uniform grid was used for $Ra = 10^4$, 10^5 and 10^6. The relaxation times for isothermal and thermal were determined by Eq. (44).

In a very recent work [32], it has been pointed out that when the IBM is used in the LBM, it can result in an artificial boundary slip whose magnitude is dependent on the relaxation time. Thus, in order to estimate the dependence of the l_2-norms on the τ_f and τ_g according to Pr in the present thermal flow problems, we have carried out the analysis of the l_2-norm in the velocity and the temperature at the immersed boundary points according to Pr.
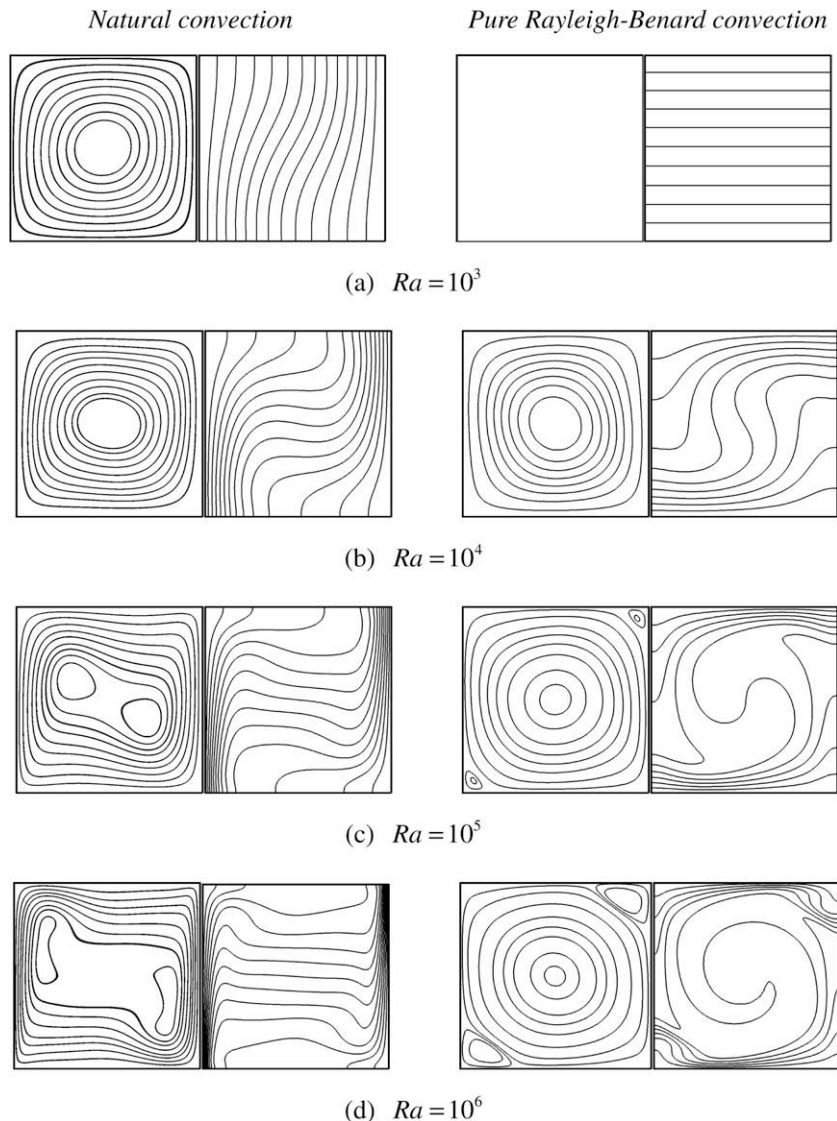

Natural convection   Pure Rayleigh-Benard convection

(a) $Ra = 10^3$

(b) $Ra = 10^4$

(c) $Ra = 10^5$

(d) $Ra = 10^6$

Fig. 4. Streamlines and Isotherms for different Rayleigh numbers ($Ra = 10^3$–10^6). (Left : Natural convection, Right : Pure Rayleigh convection)
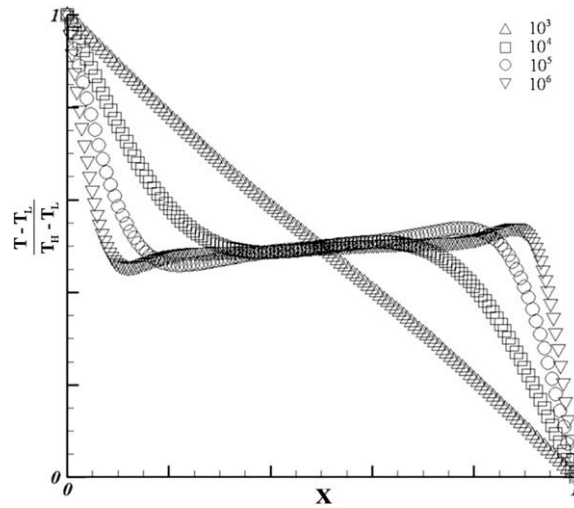
Fig. 5. Normalized temperature profiles at $y/L = 0.5$ for different Rayleigh numbers ($\triangle$: 10^3, $\square$: 10^4, $\bigcirc$: 10^5, $\triangledown$: 10^6).

Table 1
Comparison of the present calculation for surface-averaged Nusselt number at the hot wall with the previous results in vertical enclosure (VE) and horizontal enclosure (HE).

	Ra	Surface averaged Nusselt number at the hot wall ($\overline{Nu}$)				
		Present	Ref. [22]	Ref. [23]	Ref. [24]	Difference (%)
VE	10^3	1.118	1.118	1.117	1.118	0
	10^4	2.249	2.243	2.235	2.246	+0.13
	10^5	4.553	4.519	4.504	4.525	+0.61
	10^6	8.767	8.800	8.767	8.821	−0.61
HE	10^3	1.000	–	–	1.00	0
	10^4	2.170	–	2.195	2.16	+0.46
	10^5	3.925	–	–	3.91	+0.38
	10^6	6.329	–	–	6.30	+0.46

Fig. 7 shows the l_2-norms in the velocity ($l_{2,V}$) and the temperature ($l_{2,T}$) according to Pr on the immersed boundary points at $Ra = 10^4$. The $l_{2,V}$ and $l_{2,T}$ at the immersed boundary points are defined as, respectively,

$$l_{2,V} = \sqrt{\frac{1}{N_b} \sum_{n=1}^{N_b} \left[(u_n - u_d)^2 + (v_n - v_d)^2 \right]}, \tag{46}$$

$$l_{2,T} = \sqrt{\frac{1}{N_b} \sum_{n=1}^{N_b} (T_n - T_d)^2}, \tag{47}$$

where $\mathbf{u}_n = (u_n, v_n)$ and T_n are the velocity and the temperature on nth Lagrangian point at the immersed boundary, respectively, and $\mathbf{u}_d = (u_d, v_d)$ and T_d are the desired velocity and the desired temperature at the immersed boundary, respectively.

The magnitude of both l_2-norms of $l_{2,V}$ and $l_{2,T}$ decreases with increasing Pr as shown in Fig. 7. This indicated the no-slip boundary condition of velocity and the isothermal condition at the immersed boundary do not satisfy well when Pr becomes smaller in the range of Pr considered in this study. Since Pr governs the relaxation times of τ_f and τ_g as defined in Eq. (44), the magnitude of τ_f and τ_g on the l_2-norms of $l_{2,V}$ and $l_{2,T}$ according to Pr can be measured from the Table 2. With decreasing Pr, the l_2-norms increase as shown in Fig. 7, simultaneously, τ_f diminishes and τ_g augments as shown in Table 2. In the present thermal flow problems, the effect of τ_g on the l_2-norms is dominant rather than τ_f. Consequently, when τ_g as one of relaxation times in the double population function becomes relatively large in the present thermal flow problems, the l_2-norms become large, which means that the artificial boundary slip and the artificial boundary temperature on the immersed boundary become noticeable. This result is consistent with the findings of Le and Zhang [32].

The values of the relaxation times of τ_f and τ_g used in this study are small enough to neglect the artificial boundary slip and the artificial boundary temperature as revealed in Table 3, which can be guaranteed by above analysis of the l_2-norms.
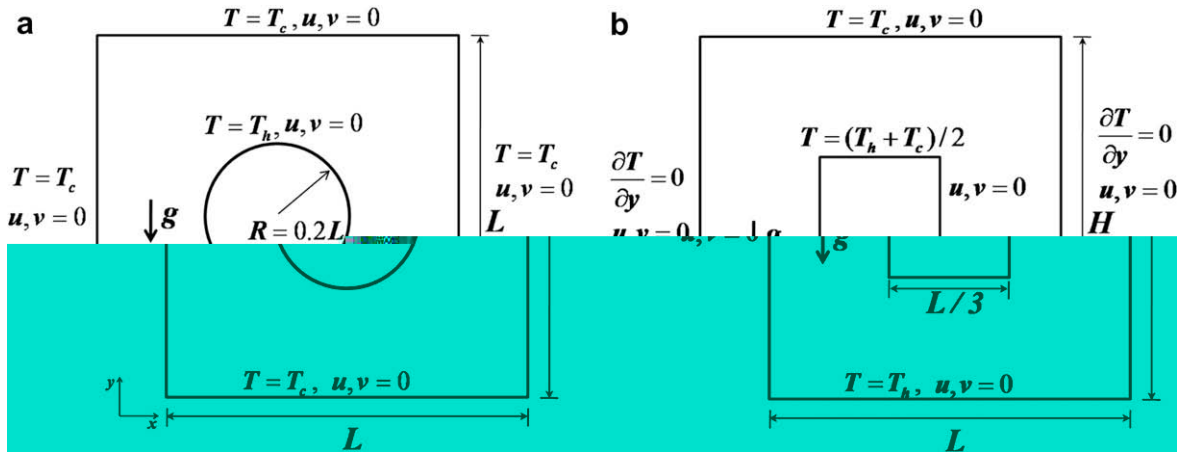
Fig. 6. Description of computational domain and boundary conditions for two different cases: a circular cylinder (a), and a square body (b) in a square enclosure.
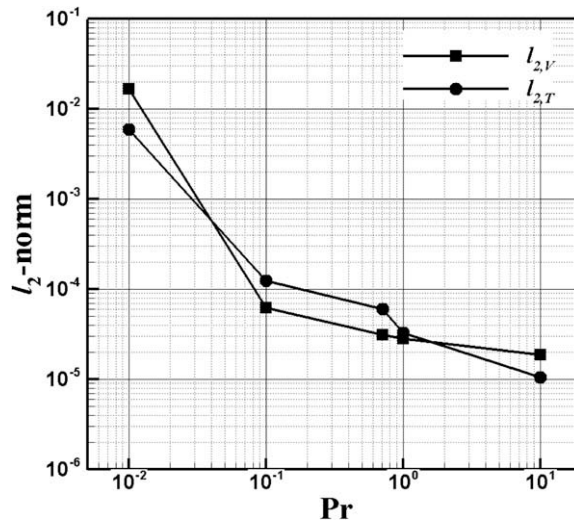

Fig. 7. l_2-norms in the velocity ($l_{2,V}$) and the temperature ($l_{2,T}$) according to Pr for the natural convection with a circular cylinder in a square enclosure at $Ra = 10^4$.

Table 2
Relaxation times and l_2-norms corresponding to Pr.

Ra	Pr	V_c	τ_f	τ_g	$l_{2,V}$	$l_{2,T}$
10^4	0.01	0.1	0.03	1.5	1.679×10^{-2}	5.906×10^{-3}
10^4	0. 1	0.1	0.095	0.474	6.246×10^{-5}	1.240×10^{-4}
10^4	0.71	0.1	0.253	0.178	3.089×10^{-5}	6.033×10^{-5}
10^4	1	0.1	0.3	0.15	2.825×10^{-5}	3.252×10^{-5}
10^4	10	0.1	0.948	0.047	1.882×10^{-5}	1.049×10^{-5}

It is well known that the role of α_f is to produce the natural oscillation of the response enforcing the no-slip boundary condition at each immersed boundary points, while β_f plays a role in damping the oscillation of the response. But, there is no general rule to determine the optimum values of α_f and β_f, regardless of the problems, because the values of α_f and β_f significantly depend on the simulation conditions such as the numerical methods and the boundary conditions. Thus, there are few researches to find the effect of these conditions on the selection of the values of α_f and β_f. Representatively, Lee [25] has investigated the stability characteristics to derive a guideline for selecting α_f and β_f when various time

advancing schemes and the corresponding stability limit of the feedback forcing immersed boundary method. Also, Saiki and Biringen [24] examined the response of the feedback forcing on the immersed boundary points for combination of α_f/β_f. They reported l_2-norm error of the velocity at the boundary points about the no-slip boundary condition with time.

Thus, in order to determine the possible range of the forcing constants, we have considered the stability conditions [25] and the characteristics of the response [24] corresponding to α_f/β_f and α_g/β_g both flow and thermal fields. As a result, $\alpha_f = -10^{-4}$ and $\beta_f = -6 \times 10^{-7}$ for momentum forcing and $\alpha_g = -10^{-4}$ and $\beta_g = -6 \times 10^{-7}$ for internal energy forcing have been selected for all the present simulations.

Fig. 8 compares the isotherms and streamlines obtained by the present study using the present method and the finite volume method with an immersed boundary method given by Kim et al. [39]. Very good agreement is achieved in the

Table 3
Relaxation times corresponding to non-dimensional parameters and characteristic velocity.

Ra	Pr	V_c	τ_f	τ_g
10^3	0.71	0.01	0.079937	0.056294
10^4	0.71	0.1	0.505569	0.356034
10^5	0.71	0.1	0.159875	0.112588
10^6	0.71	0.1	0.050557	0.035603

(a) $Ra = 10^3$

(b) $Ra = 10^4$

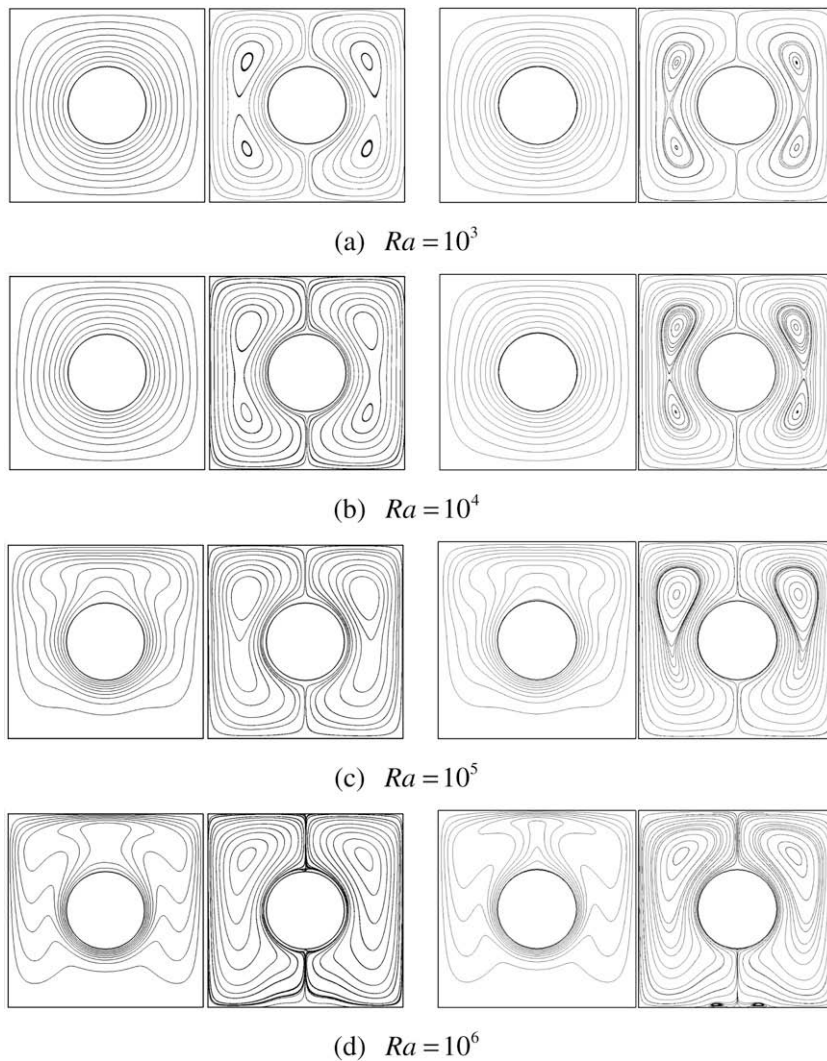(c) $Ra = 10^5$

(d) $Ra = 10^6$

Fig. 8. Comparison of isothermals and streamlines for four different Rayleigh numbers in case of a circular cylinder in a square enclosure. (left: present method, right: Ref. [25]).

patterns of the isotherms and the location of the center of vortices. For all Rayleigh numbers, the isotherms and streamlines are perfectly symmetric shape on the centerline of the square enclosure. Warm fluid heated from a circular cylinder wall rises and spreads out over the top cold walls. After the flow reaches near the top cold wall, it makes the descending current along the cold side wall toward bottom cold wall. Owing to the regularly spaced roll cells circulating in the clockwise direction at the right side and counter-clockwise direction at the left side on the centerline of the square enclosure.

For $Ra = 10^3$, the heat transfer in the enclosure is mainly dominated by the conduction mode. The circulation of the flow shows two overall rotating symmetric eddies with two inner vortices respectively as shown in Fig. 8(a) for the streamlines. At $Ra = 10^4$, the patterns of the isotherms and streamlines are about the same as those for $Ra = 10^3$. However, a careful observation indicates that the thermal boundary layer on the opposite side and the inner lower vortex slightly becomes smaller in size and weaker in strength compared with the upper one, because the effect of convection on heat transfer and flow increases with increasing the Rayleigh number. As the Rayleigh number increase up to $Ra = 10^5$, the role of convection in heat transfer becomes more significant and consequently the thermal boundary layer on the surface of the inner cylinder becomes thinner. Also, a plume starts to appear on the top of the inner cylinder and as a result the isotherms move upward, giving rise to a stronger thermal gradient in the upper part of the enclosure and a much lower thermal gradient in the lower part. In consequence, the dominant flow is in the upper half of the enclosure, and correspondingly the core of the recirculating eddies is located only in the upper half. At this Rayleigh number, the flow field undergoes a bifurcation where two inner vortices merge. The flow at the bottom of the enclosure is very weak compared with that at the middle and top regions, which suggests stratification effects in the lower regions of the enclosure. At $Ra = 10^6$, the heat transfer in the enclosure is mainly governed by the convection mode. Since the convection velocity significantly increases with increasing Rayleigh number, the boundary layer behavior can be clearly observed in regions of the lower part of cylinder and the upper part of the enclosure as shown in isotherms of Fig. 8(d). The thermal boundary layer separates from the surface near the top of the cylinder and as a result a strong plume appears. As a result, the flow strongly impinges on the top of the enclosure, which also leads to form a thinner thermal boundary layer in this region and enhances the heat transfer. Tiny symmetric vortices appear in the vicinity of the bottom wall of the enclosure owing to the separation of the boundary layer by the strong convective flow.

Table 4 shows the present numerical results together with those of previous numerical results at $Ra = 10^3 - 10^6$. Kim et al. [39] solved this problems using Navier–Stokes equations with the immersed boundary method. Shu and Zhu [40] solved this problem using the differential quadrature (DQ) method. Taylor-series-expansion and least-squares-based LBM was applied

Table 4
Comparison of the present calculation for surface-averaged Nusselt number at a cylinder surface with the previous results.

Ra	Surface averaged Nusselt number at a cylinder surface ($\overline{Nu}$)					
	Present	Ref. [39]	Ref. [40]	Ref. [41]	Ref. [42]	Difference (%)
10^3	3.399	3.396	–	–	–	
10^4	3.412	3.414	3.24	3.24	3.331	2.432
10^5	5.176	5.138	4.86	4.84	5.08	1.889
10^6	9.171	9.39	8.9	8.75	9.374	2.165

Fig. 9. Time history of surface-averaged Nusselt number at the hot wall. ($V_c = 0.1$ at all cases).

by Peng et al. [41] to simulate this natural convection problem. Moukalled and Acharya [42] solved the Navier–Stokes equations using a control volume-based numerical simulation in a body fitted coordinate. All these results are in good agreement with the benchmark results.

3.2.2. Natural convection in a square enclosure with a square body

In this study, we observed the fluid flow and thermal fields for the natural convection in an enclosure with a square body at the centre. A schematic of a two-dimensional geometry with uniform grid distribution is shown in Fig. 6(b). The system consists of a square enclosure with sides of length L and a stationary square body with side of length $L/3$ is centred. The bottom wall is kept at a constant high temperature of T_h, whereas the top wall is kept at a constant low temperature of T_c. The square body is kept at a constant a half of high temperature of $T_m = (T_h + T_c)/2$. The left and right side walls are adiabatic. Boussinesq approximation and characteristic velocity owing to the gravitational acceleration, Rayleigh number and Prandtl number were defined by the same manner with previous calculation about natural convection flow in a square enclosure with a circular cylinder. The Rayleigh number varies 10^3-10^5. The characteristic velocity and grid resolution are fixed at $V_c = 0.1c$ and 101×101 for all Rayleigh numbers. Also the relaxation times for isothermal and thermal were determined by Eq. (44). For all Rayleigh numbers considered in this study, the flow and thermal fields eventually reach steady state as shown in Fig. 9. The non-dimensional time (t^*) is defined as a diffusion time scale in Eq. (48)

$$t^* = \frac{V_c t}{L} \sqrt{\frac{Pr}{Ra}}$$

(48)

(a) $Ra = 10^3$

(b) $Ra = 4 \times 10^3$
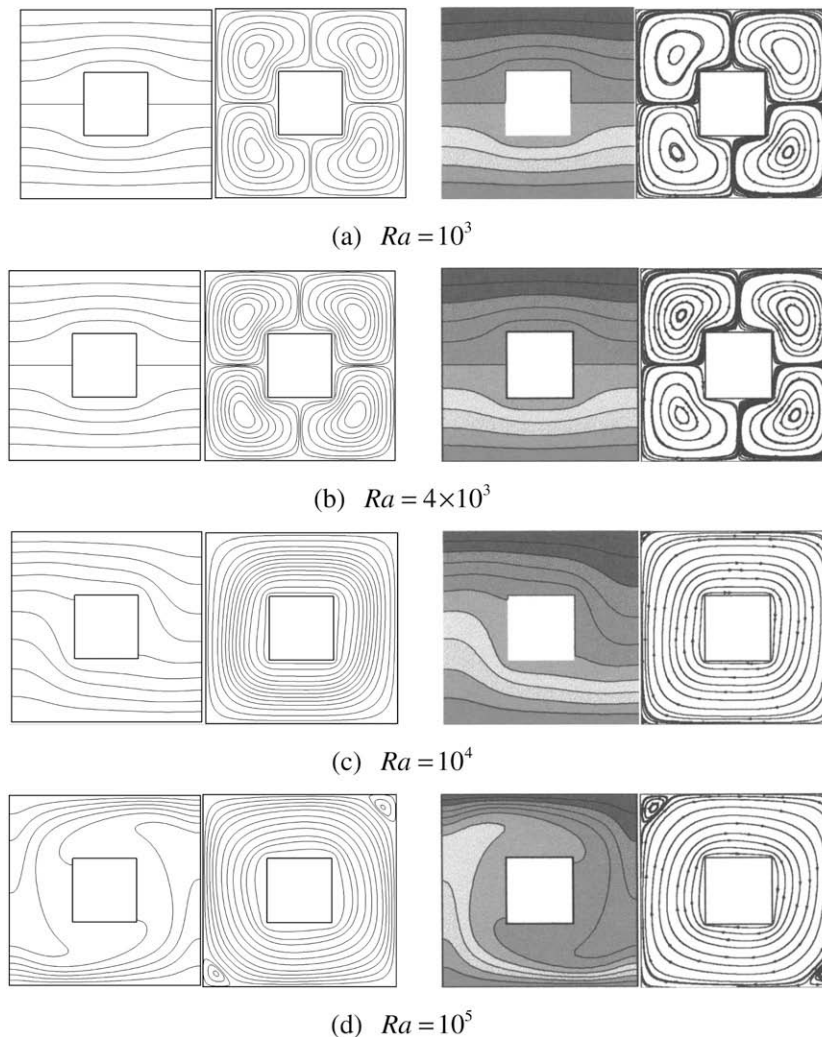
(c) $Ra = 10^4$

(d) $Ra = 10^5$

Fig. 10. Comparison of isothermals and streamlines for four different Rayleigh numbers in case of a square cylinder in a square enclosure. (left: present method, right: Ref. [29]).

Fig. 10 compares the isotherms and streamlines obtained by the present study using the present method and the spectral multi-domain method with high accuracy given by Ha et al. [43]. Very good agreement is achieved in the patterns of the isotherms and the location of the center of vortices. When $Ra = 10^3$ and 4×10^3, the values of isotherms at the lower part $(-0.5 < y < 0)$ are in the range of 0.5–1, and those at the upper part $(0 < y < 0.5)$ are in the range of 0–0.5 as shown in Fig. 10(a) and (b). The thermal gradient in the upper half of the enclosure is symmetric to that in the lower half and there is also a left-right symmetry and the vertical centreline. Thus the streamlines at $Ra = 10^3$ and 4×10^3 form four symmetric vortices circulating in the clockwise and counter-clockwise directions. The direction of rotation of these cells is uniquely determined by the thermal boundary condition. Owing to top–bottom symmetry away from the square body, the temperature along the centreline $(y = 0)$ is dictated to be $T = T_m$, while the temperature on top of the square body is held fixed at $T = T_m$. Thus, as we move away from the body at the same elevation as the top of the body, the temperature can be seen to decrease. This explains ascending flow on top of the square body, with the corresponding upward return flow away from the body for $y > 0$. Similar argument can be used to explain the descending flow below the square body with the corresponding upward return flow in the interior for $y < 0$.

When the Rayleigh number increases to $Ra = 10^4$, the symmetric shapes about $x = 0$ and $y = 0$ of isotherms and streamlines at $Ra = 10^3$ and 4×10^3 are broken and changed their shapes to diagonally symmetric ones. The four vortices formed at $Ra = 10^3$ and 4×10^3 merge with a single cell at $Ra = 10^4$. The streamline circulates in the clockwise direction, due to the presence of bottom hot and top cold walls. Because the isotherms follow the flow fields, the hot fluid at the left corner of the bottom hot wall is lifted and moves upward along the left channel between the body and left adiabatic wall. If the ascending flow meets the cold top wall and moves along the top channel between the top cold wall and the body, it is cooled by the presence of the top cold wall. The cooled heavier fluids moves downward through the right channel between the body and the right adiabatic wall, under the similar mechanism of ascending flow at the left channel. Thus the gradient of isotherms increases along the left channel and decreases along the right channel, with increasing elevation from the bottom wall.

When the Rayleigh numbers increase to 10^5, the fluid flow and temperature fields reach the final steady state after starting oscillatory transients. Thus the isotherms and streamlines in Fig. 10(d) show the temperature and velocity fields at the final steady state at $Ra = 10^5$. Since the isotherms follow the main flow circulating in the clockwise direction, the isotherms at $Ra = 10^5$ rotate further and become more tilted in the flow direction, due to increasing clockwise convective velocity with increasing Rayleigh number, compared with those at $Ra = 10^4$. Thus the thermal gradients become sharper at the top cold and bottom hot walls, giving increasing heat transfer rates at those walls with increasing Rayleigh number. The locations, where the thermal gradients are highest, moves from the left top and right bottom corners to the center of the top and bottom walls, due to the rotation of isotherms with increasing Rayleigh numbers, as shown in Fig. 10(d). The isotherms at the central core region at $Ra = 10^5$ are better mixed with decreasing thermal gradient than that at $Ra = 10^4$. Due to the increasing intensity of main clockwise vortex at $Ra = 10^5$, the size of the secondary counter-clockwise vortices at the left top and right bottom corners increases. Thus the gradient of isotherms at the left top and right bottom corners increases. Thus the gradient of isotherms at the left top and right bottom corners decrease and the isotherms at the top and bottom walls approach the symmetric shape about the vertical centreline.

Fig. 11 shows comparison the surface-averaged Nusselt number at the hot bottom wall and cold top wall with the previous results [43] for different Rayleigh numbers. The surface-averaged Nusselt number at $Ra = 4 \times 10^3$ is almost same as
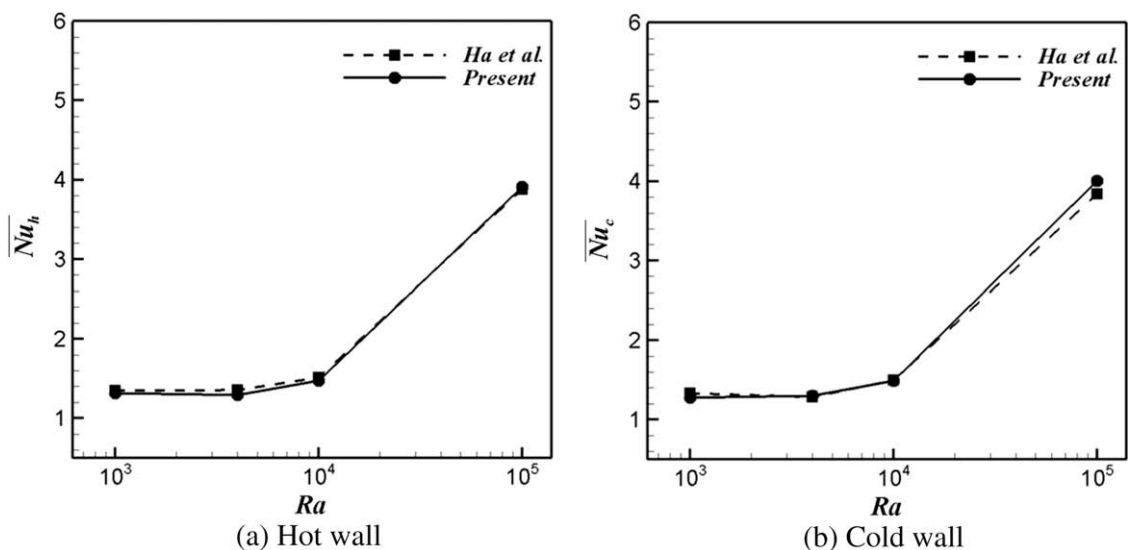

(a) Hot wall (b) Cold wall

Fig. 11. Comparison of the present calculation for surface-averaged Nusselt number at a hot wall (a) and cold wall (b) with the previous results.
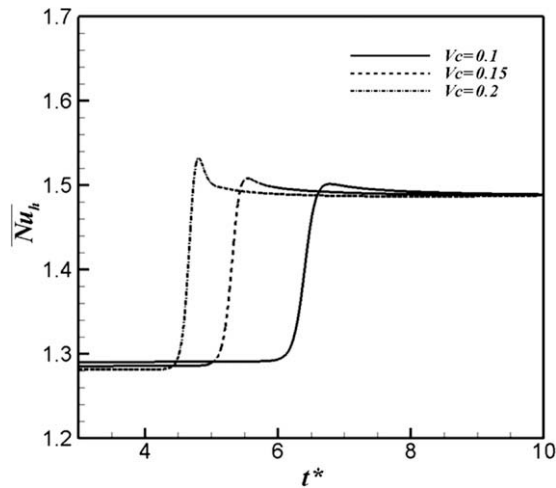
Fig. 12. Time history of surface-averaged Nusselt number at the hot wall for various characteristic velocity at $Ra = 10^4$.

that at $Ra = 10^3$, because the flows and isotherms maintain their symmetric shapes. When $Ra = 10^4$, the distribution of flow around a hot wall does not maintain the symmetric patterns and the isotherms have a strong gradient at the hot and cold walls. The surface-averaged Nusselt number at hot and cold walls increases generally due to increasing strength of convection with increasing Rayleigh number. The general trend of the surface-averaged Nusselt number at the cold wall is similar to that at the hot wall.

The CPU time (s) spent in the present method on the P4 2.41G personal computer with Windows XP operation system is given. A total CPU time is about 39,965 s up to 300,000 iterations when the numbers of the lattices and the IB points (N_b) are 40,000 and 1998, respectively. The CPU time spent to solve immersed boundary is about 343.67 s, resulting in only about 1% of the total CPU time.

3.2.3. Effect of the characteristic velocity for natural convection flow with a square body

The characteristic velocity (V_c) contains the effect of gravitational acceleration, thermal expansion, characteristic length and temperature difference between the hot and cold wall. After we find the proper characteristic velocity, the Rayleigh number can be defined by the characteristic velocity and Prandtl number. The characteristic velocity plays role of the major parameter to represent the thermal expansion and characteristics of the thermal flow. Most researchers carefully choose the characteristic velocity with the increase of the Rayleigh number beyond the incompressible limit. From this study, we can find the influence of the characteristic velocity inside the square cavity for natural convection flow. As shown in Fig. 9, for $Ra = 10^4$, the surface-averaged Nusselt number at the hot wall maintains the value of $Ra = 10^3$ or $Ra = 4 \times 10^3$, and then after $t^* = 6$, it jumps up suddenly. It means the flows near a single square body in the enclosure form four symmetric vortices circulating in the clockwise or counter-clockwise direction before $t^* = 6$. After $t^* = 6$, the flows start the secondary flow developing and make a large circulation on a square body finally. The temperature distribution is changed as flow motion and Nusselt number at the hot wall will be changed. After the flow formation is changed fully, the flows are stabilized and Nusselt number at the hot wall maintains the steady state. However, if the characteristic velocity will be changed, a point of time to start the secondary flow developing will be changed. We can confirm this phenomenon in Fig. 12. Time history of surface-averaged Nusselt number at the hot wall for various characteristic velocities at $Ra = 10^4$ was shown in Fig. 12. All the parameters and the number of grid nodes are the same for each case except for the characteristic velocity. As shown in Fig. 12, the characteristic velocity increases, as the secondary flow developing occurs earlier and the computational time decreases. However there is undesired overshoot at the end of secondary flow developing. This overshoot decreases, as the characteristic velocity increases. When we defined the characteristic velocity smaller than 0.2, the numerical instability may be increased.

Because the single internal energy relaxation time is influenced by the characteristic velocity, thermal diffusivity will be increased. Therefore the flow and temperature field are changed rapidly in comparison to the case of small characteristic velocity. Conversely, when the characteristic velocity decreases, the undesired overshoot decreases and computational time may be increase. From these characteristics of the characteristic velocity, we can find that the characteristic velocity is related with the numerical stability and computational time.

4. Conclusions

In the present study, the immersed boundary method is implemented in the thermal lattice Boltzmann method. A new approach, called Immersed boundary-thermal lattice Boltzmann method, which used the equilibrium velocity and the

equilibrium internal energy density to combine the two different grid systems, an Eulerian grid for the flow domain and a Lagrangian grid for the immersed boundary points in the flows with heat transfer, has been developed.

In order to calculate the thermal fields without bluff body, the thermal lattice Boltzmann method with the double population model has been used to simulate the natural convection in a square cavity and pure Rayleigh–Bénard convection result in giving a good agreement with previous results.

In case of heat transfer with bluff body, the heat source term from the immersed boundary method could be simply translated to the equilibrium internal energy density. Without the additional external force and heat source term during the collision calculation, this approach can maintain the advantages of the thermal lattice Boltzmann method and handle the immersed boundary points.

The natural convections in a square enclosure with circular and square body were simulated and compared with those of previous results. The numerical results agreed well with the benchmark data.

References

[1] S. Chen, G.D. Doolen, Lattice Boltzmann method for fluid flows, Ann. Rev. Fluid Mech. 30 (1998) 329.
[2] G. McNamara, B. Alder, Analysis of the lattice Boltzmann treatment of hydrodynamics, Physica A 194 (1993) 218.
[3] F.J. Alexander, S. Chen, J.D. Sterling, Lattice Boltzmann thermohydrodynamics, Phys. Rev. E 47 (1993) R2249.
[4] Y. Chen, H. Ohashi, M. Akiyama, Thermal lattice Bhatnagar–Gross–Krook model without nonlinear deviations in macrodynamic equations, Phys. Rev. E 50 (1994) 2776.
[5] A. Bartoloni, C. Battista, S. Cabasino, LBE simulation of Rayleigh–Bénard convection on the APE100 parallel processor, Int. J. Mod. Phys. C 4 (1993) 993.
[6] X. Shan, Simulation of Rayleigh–Bénard convection using a lattice Boltzmann method, Phys. Rev. E 55 (1997) 2780.
[7] X. He, S. Chen, G.D. Doolen, A novel thermal model for the lattice Boltzmann method in incompressible limit, J. Comput. Phys. 146 (1998) 282.
[8] X. He, L.S. Luo, M. Dembo, Some progress in lattice Boltzmann method. Part 1. Nonuniform mesh grids, J. Comput. Phys. 129 (1996) 357.
[9] C. Shu, Y.T. Chew, X.D. Niu, Least-squares-based lattice Boltzmann method: a meshless approach for simulation of flows with complex geometry, Phys. Rev. E 64 (2001) 045701.
[10] M. Bouzidi, M. Firdaouss, P. Lallemand, Momentum transfer of a lattice-Boltzmann fluid with boundaries, Phys. Fluids 13 (2001) 3452.
[11] R. Mei, L-S. Luo, W. Shyy, An accurate curved boundary treatment in the lattice Boltzmann method, J. Comput. Phys. 155 (1999) 307.
[12] D. Yu, R. Mei, W. Shyy, A unified boundary treatment in lattice Boltzmann method (2003) AIAA 2003-0953.
[13] I. Ginzburg, D. Humières, Multireflection boundary conditions for lattice Boltzmann models, Phys. Rev. E 68 (2003) 066614.
[14] H. Chen, C. Teixeira, K. Molvig, Realization of fluid boundary conditions via discrete Boltzmann dynamics, Int. J. Mod. Phys. C 9 (1998) 1281.
[15] R. Verberg, A.J.C. Ladd, Accuracy and stability of a lattice-Boltzmann model with subgrid scale boundary conditions, Phys. Rev. E 65 (2001) 016701.
[16] M. Rohde, J.J. Derksen, H.E.A. Van den Akker, Volumetric method for calculating the flow around moving objects in lattice-Boltzmann schemes, Phys. Rev. E 65 (2002) 056701.
[17] C.S. Peskin, Flow patterns around heart valves: a numerical method, J. Comput. Phys. 10 (1972) 252.
[18] C.S. Peskin, The fluid dynamics of heart valves: experimental, theoretical, and computational methods, Ann. Rev. Fluid Mech. 14 (1982) 235.
[19] Peskin, The immersed boundary method, Acta Numer. 11 (2002) 479.
[20] Mittal, Iaccarino, Immersed boundary methods, Annu. Rev. Fluid Mech. 37 (2005) 239.
[21] D. Goldstein, R. Handler, L. Sirovich, Modeling a no-slip flow boundary with an external force field, J. Comput. Phys. 105 (1993) 354.
[22] D. Goldstein, R. Handler, L. Sirovich, Direct numerical simulation of turbulent flow over a modeled riblet-covered surface, J. Fluid Mech. 302 (1995) 333.
[23] D. Goldstein, T.C. Tuan, Secondary flow induced by riblets, J. Fluid Mech. 363 (1998) 115.
[24] E.M. Saiki, S. Biringen, Numerical simulation of a cylinder in uniform flow: application of a virtual boundary method, J. Comput. Phys. 123 (1996) 450.
[25] C. Lee, Stability characteristics of the virtual boundary method in three-dimensional applications, J. Comput. Phys. 184 (2003) 559.
[26] Z.G. Feng, E.E. Michaelides, The immersed boundary-lattice Boltzmann method for solving fluid–particles interaction problems, J. Comput. Phys. 195 (2004) 602.
[27] Z.G. Feng, E.E. Michaelides, Proteus: a direct forcing method in the simulations of particulate flow, J. Comput. Phys. 202 (2005) 20.
[28] X.D. Niu, C. Shu, Y.T. Chew, A thermal lattice Boltzmann model with diffuse scattering boundary condition for micro thermal flows, Comput. Fluids 36 (2007) 273.
[29] C. Shu, N. Liu, Y.T. Chew, A novel immersed boundary velocity correction-lattice Boltzmann method and its application to simulate flow past a circular cylinder, J. Comput. Phys. 226 (2007) 1607.
[30] Y. Peng, L-S. Luo, A comparative study of immersed-boundary and interpolated bounce back methods in LBE, Prog. Comput. Fluid Dyn. 8 (2008) 156.

[41] Y. Peng, Y.T. Chew, C. Shu, Numerical simulation of natural convection in a concentric annulus between a square outer cylinder and a circular inner cylinder using the Taylor-series-expansion and least-squares-based lattice Boltzmann method, Phys. Rev. E 67 (2003) 026701.
[42] F. Moukalled, S. Acharya, Natural convection in the annulus between concentric horizontal circular and square cylinders, J. Thermophys. Heat Transfer 10 (1996) 524.
[43] M.Y. Ha, I.K. Kim, H.S. Yoon, K.S. Yoon, J.R. Lee, Two-dimensional and unsteady natural convection in a horizontal enclosure with a square body, Numer. Heat Transfer A 41 (2002) 183.